# Experimental determination of Li isotope behaviour during basalt weathering

Philip A.E. Pogge von Strandmann[1*], Wesley T. Fraser[2], Samantha J. Hammond[3], Gary Tarbuck[1], Ian G. Wood[1], Eric H. Oelkers[1], Melissa J. Murphy[1]

[1]London Geochemistry and Isotope Centre (LOGIC), University College London and Birkbeck, University of London, Gower Place, London, WC1E 6BT.

[2]Geography, Oxford Brookes University, Oxford, OX3 0BP

[3]School of Environment, Earth and Ecosystems Sciences, The Open University, Walton Hall, Milton Keynes, MK7 6AA

*Corresponding author: p.strandmann@ucl.ac.uk

Abstract

Silicate weathering is the primary control of atmospheric $CO_2$ concentrations on multiple timescales. However, tracing this process has proven difficult. Lithium isotopes are a promising tracer of silicate weathering. This study has reacted basalt sand with natural river water for ~9 months in closed experiments, in order to examine the behaviour of Li isotopes during weathering. Aqueous Li concentrations decrease by a factor of ~10 with time, and $\delta^7$Li increases by ~19‰, implying that Li is being taken up into secondary phases that prefer $^6$Li. Mass balance using various selective leaches of the exchangeable and secondary mineral fractions suggest that ~12–16% of Li is adsorbed, and the remainder is removed into neoformed secondary minerals. The exchangeable fractionation

factors have a $\Delta^7Li_{exch\text{-}soln}$ = -11.6 to -11.9‰, while the secondary minerals impose $\Delta^7Li_{secmin\text{-}soln}$ = -22.5 to -23.9‰. Overall the experiment can be modelled with a Rayleigh fractionation factor of $\alpha$ = 0.991, similar to that found for natural basaltic rivers. The mobility of Li relative to the carbon-cycle-critical cations of Ca and Mg changes with time, but rapidly evolves within one month to remarkably similar mobilities amongst these three elements. Th evolution shows a linear relationship with $\delta^7Li$ (largely due to a co-variation between aqueous [Li] and $\delta^7Li$), suggesting that Li isotopes have the potential to be used as a tracer of Ca and Mg mobility during basaltic weathering, and ultimately $CO_2$ drawdown.

## 1.0 Introduction

Chemical weathering of continental silicate rocks is one of the primary drivers of the long-term carbon cycle and climate (Chamberlin, 1899; Walker et al., 1981). Weathering provides nutrients to the ocean to fertilise primary productivity, clay particles to help bury organic carbon (Hawley et al., 2017), and, critically, alkalinity and cations such as Ca and Mg for the precipitation of marine carbonate (Berner et al., 1983). All of these processes sequester atmospheric $CO_2$ on various timescales, making chemical weathering a fundamental Earth climate system process.

Significant effort has gone into understanding and quantifying silicate weathering, both in the present (e.g. Maher, 2011; West et al., 2005), and in the geological past (e.g. Foster and Vance, 2006; Pogge von Strandmann et al., 2017a; Vance et al., 2009). Traditionally, marine radiogenic strontium isotopes have been used to determine past weathering changes (McArthur et al., 2001), but

51 their interpretation is far from unambiguous, because seawater isotope ratios
52 are impacted by hydrothermal inputs and riverine isotope ratios are strongly
53 dependent on the lithology undergoing weathering. This is further complicated
54 by the inability to distinguish between carbonate and silicate weathering, where
55 only the latter draws down $CO_2$ on the long-term (Allegre et al., 2010; Oliver et
56 al., 2003). Hence, other tracers have been sought – ideally ones that are relatively
57 unaffected by lithology, by carbonate weathering (which does not affect $pCO_2$ on
58 $>10^4$ year timescales) or by biology and plant growth. So far, the only tracer that
59 meets all these criteria is lithium isotopes.
60 Lithium isotopes (reported as $\delta^7Li$, the ‰ deviation from a normalising
61 standard) are unaffected by carbonate weathering, because silicates are orders
62 of magnitude more concentrated in Li than carbonates (Kisakürek et al., 2005;
63 Millot et al., 2010; Pogge von Strandmann et al., 2017b), or by plant growth or
64 primary productivity (Lemarchand et al., 2010; Pogge von Strandmann et al.,
65 2016). The $\delta^7Li$ range in primary silicate rocks (continental crust ~0‰; basalt
66 3–5‰ (Elliott et al., 2006; Sauzeat et al., 2015)) is narrow compared to that
67 observed in rivers draining those rocks ($\delta^7Li$ = 2–44‰, mean 23‰ (Dellinger et
68 al., 2015; Huh et al., 1998; Pogge von Strandmann et al., 2006)). This range is due
69 to the formation of secondary minerals (clays, zeolites and Fe-Mn-Al
70 oxyhydroxides) during weathering, where these minerals preferentially take up
71 the light isotope, $^6Li$, driving residual river and soil waters isotopically heavy
72 (Vigier et al., 2008; Wimpenny et al., 2010). These secondary minerals also
73 adsorb Li onto their exchangeable sites, imposing the same isotopic fractionation
74 direction (Hindshaw et al., 2019; Pistiner and Henderson, 2003). Hence, Li
75 isotopes in natural waters are controlled by the ratio of primary mineral

dissolution (low $\delta^7$Li) relative to secondary mineral formation (driving solution $\delta^7$Li high). This ratio is known as the "weathering congruency" (Misra and Froelich, 2012; Pogge von Strandmann and Henderson, 2015), which may be used as a tracer of chemical weathering intensity (Dellinger et al., 2015). Overall, this ratio also informs on the efficiency of weathering in removing $CO_2$, because if cations are being trapped by secondary minerals on the continents within clays and soils, they will not enter the ocean to form carbonate and sequester $CO_2$.

However, while the general mechanics of Li isotope fractionation during weathering are fairly well understood, there is less information available on the precise processes that $\delta^7$Li traces, such as whether the primary fractionation mechanism is adsorption onto secondary mineral surfaces, uptake into interlayer sites, or via structural or lattice-bound incorporation into neoformed minerals (Hindshaw et al., 2019; Pistiner and Henderson, 2003; Pogge von Strandmann et al., 2010; Wimpenny et al., 2015). Further, fractionation factors and reaction kinetics are also poorly known.

In this study, we react basalt with river water for around nine months in closed system experiments, following the methods of previous experiments (Jones et al., 2012). The primary goal is to examine Li isotope behaviour during these weathering experiments, to determine which phases affect Li isotopes during weathering, and to quantify their response.

## 2.0 Methods

### *2.1 Experimental methods*

Following the methods of Jones et al. (2012), approximately 250g of the natural basaltic sand used in the Jones et al. experiments was placed in 1L pre-

101 leached PTFE beakers containing 900ml of water. This sand was collected from
102 the bottom of the Borgarfjörður estuary in Iceland, and was characterised by
103 Jones et al. (2012). These data are repeated in Supplemental Table 1 for
104 completeness' sake. The sand consists of fairly fresh basalt (for example it
105 contains significant basaltic glass), but also contains small amounts of
106 phyllosilicates only just detectable by X-Ray Diffraction, as described below. For
107 the water to be naturally charge-balanced and have a natural amount of
108 alkalinity, the water used in the experiments was collected from the local Great
109 Ouse River in eastern England. While the composition of this water is not
110 identical to that in Iceland where the sand was sampled, the similarities in
111 temporal fluid concentration behaviour (described below) between this study
112 and Jones et al. (2012), which used Icelandic water, suggest that the differences
113 in these water compositions only has a minor effect on experimental results.
114 Two identical experiments were run at 20°C in a shaking bath reactor, in
115 order to determine that the Li isotope behaviour was not anomalous. Closed
116 systems were used (rather than through-flow reactors) in order to be able to
117 mass balance the reactants, and to facilitate retrieval of isotopic fractionation
118 factors. Trace element concentrations were only determined from one of the
119 experiments. At periodic intervals, the water pH was measured, and 50 ml of
120 water was removed and filtered through 0.2μm cellulose acetate syringe filters,
121 and stored in pre-cleaned PTFE bottles. Sampling frequency was initially daily,
122 but decreased throughout the experiment (Table 1).
123 Post-experiment, the reacted basalt was dried and stored. The pre- and
124 post-experimental basalts were also leached, to examine their exchangeable
125 fraction. This leach followed the Tessier method, by leaching the basalt in 1M

sodium acetate for 1 hour at room temperature (Hindshaw et al., 2019; Pogge von Strandmann et al., 2013; Tessier et al., 1979). Following this, the residue was leached for 1 hour with 0.6M HCl, which attacks the secondary mineral fraction, i.e. clays as well as oxyhydroxides and zeolites (Pogge von Strandmann et al., 2014; Tessier et al., 1979). Bulk basalt was dissolved in a standard method of concentrated HF-$HNO_3$-$HClO_4$, followed by $HNO_3$ and 6M HCl.

*2.2 XRD and FTIR methods*

X-ray powder diffraction analysis was carried out on a "whole sample" basis. Samples were prepared by grinding the material under ethanol using an agate pestle and mortar and the dried powder was side-filled against a ground-glass surface into a rectangular sample holder 20 x 20 mm in area and 1.5 mm deep. Diffraction patterns were collected with Co radiation, using a PANalytical X'Pert Pro diffractometer with Bragg-Brentano parafocusing reflection geometry. This instrument is equipped with a Ge(1 1 1) Johansson-type focusing monochromator, producing a CoK$\alpha_1$ incident beam. The X-ray tube was operated at 40 kV and 30 mA. Variable-width divergence and anti-scatter slits were used, together with a 15 mm wide beam mask in the incident beam, so as to illuminate a constant 15mm × 15mm area of the sample; 0.04 radian Soller slits were present in both the incident and diffracted beams to reduce the axial divergences. The X-ray detector was an "X'Celerator" position-sensitive detector; this device covers an angular range in 2θ of ±1.061°, with an effective fixed step size of 0.0167°. Data were collected over the 2θ range from 5° to 70° (20.5 Å < *d* < 1.56 Å), with data collection times of 15 hours.

Fourier-transform infrared (FTIR) analyses were conducted on dried samples using a Perkin-Elmer Spectrum2 (Seer Green, Buckinghamshire, UK) attenuated total reflectance-FTIR (ATR-FTIR) spectrometer, fitted with a single-bounce diamond ATR cell. A total of 8 scans were used to generate an average spectrum for each sample at a resolution of 4$cm^{-1}$. Spectra spanned the range 4000-600 $cm^{-1}$. All samples were analysed in triplicate.

Clay minerals typically show a pronounced broad absorption band centred at c.3300$cm^{-1}$ associated with hydroxyl (OH) groups interacting via hydrogen bonding within the clay structure, thus an increase in OH spectral response indicates an increase in clay mineral content of a sample.

*2.3 Concentration analyses*

The solution concentrations were analysed at The Open University, using an Agilent 8800 triple quadrupole inductively coupled plasma mass spectrometer (ICP-QQQ-MS). The instrument has two quadrupole mass filters, which are separated by a collision / reaction cell (allowing targeted interference removal in the cell). We ran in two modes of analysis, no gas for Li (as no interference ions are present on mass) and in He collision mode for all other analytes. In no gas mode, oxide levels (measured as $CeO^+/Ce^+$) were at 0.96% and doubly charged species ($Ce^{2+}/Ce^+$) at 1.80%. In He mode, these were at 0.44% and 1.30% respectively.

Prior to analysis, samples were diluted 10 fold from the original solution in 2% $HNO_3$ to allow analysis of all masses in the same analytical session. Analyses were calibrated against a suite of synthetic multi-element solutions, which were made up to cover the range of concentrations in the experimental

175 solutions. An on-line internal standard (Rh and In) was added to each sample
176 and standard also, to monitor and correct for instrument drift. In addition, drift
177 was further monitored by running a measurement block consisting of the
178 original water used in the experiments, one of the calibration standards and a
179 2% $HNO_3$ blank every 5 – 6 unknowns (5 times during the analytical session).
180 Where concentrations are above the detection limit in the initial water,
181 reproducibility is better than 2.5% (relative standard deviation from the mean of
182 the five measurements). Accuracy was also determined using the international
183 river water reference standard SLRS-5, and was within uncertainty of certified
184 values. Lithium and silicon are not certified in SLRS-5, so in this case we
185 compared to published concentrations and were also within uncertainty
186 (Heimburger et al., 2013).
187 Major elemental concentrations of the starting basalt are taken from
188 Jones et al. (2012), except for Li concentrations, which were determined by ICP-
189 MS analyses in a similar manner to the dissolved concentrations, while running
190 BCR-2 as an external standard, whose values were within uncertainty (±6%) of
191 isotope-dilution determined Li concentrations in BCR-2 (Pogge von Strandmann
192 et al., 2011). All concentrations are reported in the Supplement.
193 The elemental ratios of the leachates were determined using a Varian
194 720ES ICP-OES. Samples were calibrated using matrix-matched synthetic
195 standards (i.e. in Na acetate and dilute HCl).
196
197
198 *2.4 Li isotope analyses*

199 Approximately 15ml of water was evaporated, and passed through a two-
200 stage cation exchange column procedure, using AG50W X-12 resin, and eluting
201 with dilute HCl (Pogge von Strandmann et al., 2011). Column splits were
202 collected before and after the main elute, and analysed for Li content, to
203 determine how much Li was in the sample. Using this method, it was determined
204 that >99.9% of sample was collected in the main column elution.
205 Purified samples were analysed using a new Nu Plasma 3 multi-collector ICP-MS
206 at the LOGIC laboratories. A sample-standard bracketing procedure was used
207 relative to the IRMM-016 standard. Each sample was measured three separate
208 times during an analytical procedure, repeat measurements being separated by
209 several hours, but during the same analysis session. Each individual
210 measurement consisted of 10 ratios (50 s total integration time), giving a total
211 integration time of 150 s/sample for the three repeat measurements that
212 constitute a single analysis (n=1). We use the 2sd (standard deviation) of these
213 three measurements as an assessment of our individual uncertainty, although
214 values reported in Table 1 have also been compounded for the difference in
215 normalising standards described below.
216 This mass spectrometer has new cones (compared to previous Nu MC-
217 ICP-MSs), and, using the specific "super-lithium cones", and a Cetac Aridus 2
218 desolvation system, a 5 μg/L solution gives a signal intensity of 100–140 pA (10–
219 14V) of $^{7}Li^{+}$ at an uptake rate of ~100 μl/min. Background, instrumental Li
220 intensities, typically ~0.07 pA (7mV), were subtracted from the sample and
221 standard intensities. Total procedural blanks were generally indistinguishable
222 from background, and contain <0.003 ng Li.

223 Lithium isotope ratios are commonly reported relative to the LSVEC
224 standard (Flesch et al., 1973). LSVEC analysed relative to IRMM-016 yields $\delta^7$Li =
225 -0.003 ± 0.054 (2se, n=19), which is in close agreement with past corresponding
226 measurements (Jeffcoate et al., 2004; Phan et al., 2016). All reported $\delta^7$Li values
227 have been re-normalised to LSVEC, and the reported uncertainty has been
228 propagated to encompass analytical uncertainty on both samples, normalising
229 standards and LSVEC.
230 Given that this is the first Li isotope study published at the new LOGIC isotope
231 mass spectroscopy facilities, we have gone to some effort to determine the
232 accuracy and precision of our analyses. We have therefore analysed seawater
233 (both IAPSO and North Atlantic seawater) and the USGS rock standards BCR-2
234 (basalt), G-2 (granite), PCC-1 (peridotite) and SGR-1b (shale). Relative to LSVEC,
235 seawater $\delta^7$Li = 31.11 ± 0.38‰ (2sd; n=12) (identical to other published values,
236 e.g. Dellinger et al., 2015; James and Palmer, 2000; Jeffcoate et al., 2004; Pogge
237 von Strandmann and Henderson, 2015). Our other values also compared well to
238 published values: BCR-2: $\delta^7$Li = 2.64 ± 0.31‰ (n=5) (e.g. 2.6±0.3‰ (Pogge von
239 Strandmann et al., 2011); 2.7±1.3‰ (Liu et al., 2013); 2.9 ± 0.3‰ (John et al.,
240 2012)); G-2: $\delta^7$Li = 0.14 ± 0.16‰ (n=3) (e.g. 0.1 ± 0.8‰ (Phan et al., 2016); 0.6 ±
241 1.8‰ (Sauzeat et al., 2015)); PCC-1: $\delta^7$Li = 8.72 ± 0.13‰ (n=3) (e.g. 8.9 ± 0.4‰
242 (Magna et al., 2006)); SGR-1b: $\delta^7$Li = 4.00 ± 0.24‰ (e.g. 4.7 ± 0.7‰ (Phan et al.,
243 2016); 3.6 ± 0.4‰ (Pogge von Strandmann et al., 2017b); 4.9 ± 1.9‰ (Hindshaw
244 et al., 2018)). Hence, our standard results show that our Li isotope analyses are
245 accurate, and have a long-term external precision (for the twelve months the
246 new laboratory has been operational) of better than ±0.4‰ (2sd).

## 3.0 Results

### *3.1 Concentrations*

The same basalt sand as used by Jones et al. (2012) was also used for this experiment, and details are given in Supplementary Table 1. The Li concentration of the unreacted basalt is 5.53 μg/g, similar to MORB and other Icelandic basalts (Elliott et al., 2006; Pistiner and Henderson, 2003). The post-reaction basalts have indistinguishable bulk Li concentrations of 5.3–5.6 μg/g.

Compared to the bulk basalt composition, the sodium acetate leach (exchangeable fraction) of the unreacted basalt has considerably higher Mg/Si ratios (mass ratio $Mg/Si_{bulk\ basalt} = 0.27$, while $Mg/Si_{exch} = 25.3$) (Table 2). Silicon (as a neutral species) should not be present in the exchangeable leach, and its presence (albeit at very low concentrations) implies that the leach is not fully efficient due to a small contribution of Si from the dissolution of silicate minerals (Hindshaw et al., 2019). Lower Mg/K ratios in the exchangeable fractions ($Mg/K_{bulk\ basalt} = 13.7$, while $Mg/K_{exch} = 0.75$), and undetectable Al and Fe demonstrate that the exchangeable fraction of the initial basalt is enriched in the elements that would be expected to partition into this fraction (Renforth et al., 2015; Sigfusson et al., 2008; Tessier et al., 1979). The exchangeable fractions of the reacted basalts have somewhat lower Mg/Si (8.2–9.5). Li/Si is also several orders of magnitude higher in the unreacted exchangeable fraction than the initial bulk basalt (0.04 compared to $3 \times 10^{-5}$), and decreases slightly in the reacted basalts (0.015–0.03), showing that Li is considerably more affiliated with sorption than Si.

In contrast, the HCl leach (that should attack the secondary mineral phases) of the unreacted basalt has similar Mg/Si to the bulk basalt (0.29 compared to 0.27). However, elements that would be expected to be enriched in clays and oxyhydroxides are enriched: Al/Si is 0.63 in the leach, compared to 0.36 in the bulk basalt, while Fe/Si is 0.92 compared to 0.53. Li/Si is also over an order of magnitude higher in the leaches. The reacted basalts' leached Li/Si ratios are slightly lower than the unreacted basalt (Table 2). Overall, the leaches appear to have targeted the expected phases: the adsorbed fraction is enriched in exchangeable cations, and the secondary mineral plus Fe and Al oxyhydroxides fraction is enriched in elements such as Fe, Al and Li, as demonstrated before for basalts (Chapela Lara et al., 2017; Hindshaw et al., 2019; Opfergelt et al., 2014; Pogge von Strandmann et al., 2012; Pogge von Strandmann et al., 2014; Sigfusson et al., 2008; Tessier et al., 1979).

The concentrations of the initial unreacted water, and the experimental aqueous solutions are given in Table 1. A sample of the initial water was kept at the same conditions as the experiments (without any contact with basalt, and with atmospheric contact) to examine how the pH evolved. The initial pH of this aqueous solution started at 7.1, increased to 7.6 after a month, and then decreased to 7.3 by the end of the experiment (Table 1). Both basalt-water experiments showed the same pattern, but were consistently about 0.2 pH units lower.

Aqueous solution concentration behaviour is generally similar to that reported by Jones et al. (2012). Most major elemental concentrations increase with reaction time (Fig. 1), with an overall 3% increase in Na, 24% in Mg, 93% in Si, while at the same time K and Ca concentrations decrease slightly (on the

296 order of 10%). This behaviour for the individual elements is similar to that
297 observed by Jones et al. (2012), although the enrichment amounts vary. This is
298 likely due to the different composition of the waters used in these experiments
299 (Jones et al., 2012). Minor elements like Al and Mn also increase. Almost all of
300 these elements reach apparent steady-state (stable concentrations) after ~50–
301 100 days after the beginning of the experiments. Importantly for these
302 experiments, as also shown by Jones et al. (2012), Li concentrations decrease,
303 from 13.5 μg/L in pre-experimental water to 1.3 μg/L by the end of the
304 experiment. By comparison, the flow-weighted mean global river concentration
305 is 1.5 μg/L (Huh et al., 1998). This behaviour results in a rapid increase in some
306 elemental ratios including Mg/Na, which attains a near steady value after ~12
307 days. The Li/Na ratios evolve to a constant value more slowly, due to the more
308 gradual decline in Li concentrations.
309
310 *3.2 Li isotopes*
311 The $\delta^7$Li of the pre-experimental bulk basalt is 4.4‰, similar to other
312 Icelandic and MORB basalts (Elliott et al., 2006; Pogge von Strandmann et al.,
313 2006; Pogge von Strandmann et al., 2012; Vigier et al., 2009). The post-
314 experimental bulk basalts from the two experiments have a $\delta^7$Li of 4.1–4.5‰,
315 within analytical uncertainty of the pre-experimental basalt (Table 2).
316 The exchangeable fraction (sodium acetate leach) of the pre-experimental
317 basalt has a $\delta^7$Li of 17.8‰, with a Li concentration of 0.7 μg/L (compared to a
318 total procedural blank of 0.03 μg/L Given the presence of minor quantitites of Si
319 in these leaches from the dissolution of silicate minerals (see Section 3.1), the
320 leachate $\delta^7$Li is likely slightly lower value than if the leach were fully efficient.

The secondary mineral fraction (HCl leach) has a $\delta^7$Li of 5.3‰ with a Li concentration in the leach of 11.6 ng/g. As for the exchangeable leach, the secondary mineral leach is unlikely to have been totally efficient (Hindshaw et al., 2019), although elemental ratios in this leach (Table 2) are close to stoichiometry for some examples of smectite.

The post-experiment exchangeable fractions have $\delta^7$Li values of 21.3 and 21.8‰, while the HCl leach has $\delta^7$Li values of 9.3–10.8‰ (i.e. 4.0–5.5‰ higher than that of the unreacted pre-experimental basalt leach). Concentrations must be normalised to the amount of material in the experiment to be meaningful. Thus, exchangeable Li increases from 1.1 μg in the total (250g) pre-experiment basalt to 2.5–2.9 μg post-experiment. Similarly, the HCl leach increases from 17.6 μg to 27–27.5 μg.

The $\delta^7$Li of the initial reactive aqueous fluid is 14‰, and these fluids then exhibit an increase with time to a final value of 33.3‰ in both experiments (Fig. 2). The simultaneous decrease in Li concentrations of these fluids results in a negative correlation between $\delta^7$Li and [Li], which is frequently observed in basaltic rivers (Pogge von Strandmann et al., 2010; Pogge von Strandmann et al., 2006; Vigier et al., 2009), although natural rivers tend to have slightly lower concentrations (Fig. 3), likely due to the relatively higher [Li] in the starting solution of these experiments. In both experiments, an approximate steady-state appears to have been reached, with both Li concentrations and isotopes approximately stable for the last 125 days of the experiment.

## 4.0 Discussion

345 *4.1 Lithium mass balance*

346 The mass balance of lithium in the experiments can be used to determine
347 the destination of Li lost from the fluid. In principle there are two phases that
348 could be taking up Li from the fluid: the exchangeable fraction (i.e. sorbed Li) and
349 the secondary mineral fraction (i.e. Li substituting into the crystal structures of
350 neoforming minerals)(Chan and Hein, 2007; Millot and Girard, 2007; Pistiner
351 and Henderson, 2003; Vigier et al., 2008; Wimpenny et al., 2015; Wimpenny et
352 al., 2010). For this mass balance, we assume that the Na acetate leach represents
353 the exchangeable fraction, while the subsequent HCl leach represents Li
354 recovered from secondary minerals (including oxyhydroxides and clays or
355 zeolites).

356 We also assume that Li added to solution by primary basalt dissolution
357 can be calculated by assuming that the increase in fluid of Mg or Si represents
358 stoichiometric dissolution (Jones et al., 2012), such that the Li/Mg or Li/Si
359 concentration ratios remain constant during dissolution. Stoichiometric
360 weathering is unlikely to be a perfect assumption, given that both Mg and Si are
361 also known to partition into secondary minerals as well (e.g. (Opfergelt et al.,
362 2014; Pogge von Strandmann et al., 2012)). However, constant elemental ratios
363 during dissolution is likely a robust assumption, as Li is a moderately
364 incompatible element, and does not partition preferentially into any primary
365 basaltic minerals (Penniston-Dorland et al., 2017). In any case, the amount of Li
366 added from basalt dissolution is minor compared to that lost from solution.
367 According to the Mg and Si concentration increase, between 0.015 and 0.07 g of
368 the ~250 g basalt samples dissolved during the experiments, which is around
369 4% of the total Li mass balance (~0.4μg Li, assuming constant Li/Mg ratios).

In the experiments, when normalised to the amount of material used, the exchangeable fraction gained ~1.4–1.8μg Li, while the secondary minerals gained ~9.4–9.9 μg Li. The solution (when corrected for fluid loss due to sampling) lost ~11.4μg Li by the end of the experiment.

Given weighing errors and propagated analytical uncertainty, the experiments therefore can be mass balanced, with around ~82–87% of the Li lost from the fluid substituting into secondary phases, and ~12–16% being taken into the exchangeable fraction (Fig. 4). This result demonstrates that the sorbed fraction is of sufficient importance to be an integral consideration of future lithium weathering studies.

*4.2 Mineral saturation states*

Mineral saturation states in the fluids were calculated using the PHREEQC programme (Parkhurst and Appelo, 1999). Basaltic primary minerals (olivine, plagioclase, pyroxene) are undersaturated in all the experimental fluids, and hence are likely to dissolve. The undersaturation of these minerals is maintained by supersaturation (and hence likelihood of precipitation) of secondary minerals (Gíslason et al., 1996). For example, both kaolinite and smectite are consistently supersaturated in all the experimental solutions. However, while kaolinite's saturation is broadly constant, that of smectite increases with time. Iron oxyhydroxides (e.g. amorphous $Fe(OH)_3$, another common basaltic secondary mineral) starts out undersaturated, but becomes supersaturated after about 4 days of reaction.

Mineral saturation states provide insight into whether neoformation or sorption is dominantly controlling Li isotope fractionation. There is a clear co-

395 variation between the saturation state of smectite (Aberdeen-montmorillonite)
396 and $\delta^7$Li that does not exist for any other modelled secondary minerals. As the
397 smectite saturation state increases, so as the likelihood of precipitation
398 increases, the $\delta^7$Li also increases, because more $^6$Li is being incorporated into
399 precipitating smectites. It is also noticeable that extrapolation of the trend line
400 ($r^2 = 0.94$) back into undersaturated conditions (SI < 0) leads to the initial $\delta^7$Li
401 values of the basalts used (Fig. 5). In other words, when no smectite is forming, it
402 appears that the solutions would have an identical $\delta^7$Li value to primary basalt
403 (i.e. congruent weathering). As smectite precipitation increases, $^6$Li is
404 preferentially removed from the fluid, increasing solution $\delta^7$Li values. In
405 contrast, were Fe oxyhydroxide the dominant secondary mineral controlling Li,
406 its undersaturated conditions at the start of the experiment should result in
407 unfractionated Li isotopes, which is not observed.
408 Therefore, this confirms that clay formation strongly affects Li isotope
409 fractionation (Bouchez et al., 2013; Wimpenny et al., 2015; Wimpenny et al.,
410 2010), but also adds to the mass balance argument made above, that it is
411 secondary mineral formation, rather than sorption, that is largely controlling Li
412 isotope fractionation in this experiment (84–88% of Li by mass balance)
413 (Hindshaw et al., 2019; Pistiner and Henderson, 2003; Vigier et al., 2008;
414 Wimpenny et al., 2015).
415
416 *4.3 Li isotope fractionation*
417 Assuming that the Li concentrations and isotope ratios measured in the
418 exchangeable and secondary mineral fractions represent fractionation from the

419 youngest (most recent) experimental fluids in the dissolved fraction, it is
420 possible to calculate fractionation factors into both solid fractions.
421 The $\Delta^7Li_{exch\text{-}soln}$ of the experiments is -11.6 to -11.9‰, while the $\Delta^7Li_{secmin\text{-}}$
422 $_{soln}$ is -22.5 to -23.9‰. The weighted fractionation factor of total Li taken into
423 both fractions combined is on average ~-22‰. Iceland basaltic rivers exhibit
424 $\Delta^7Li$ values between unleached suspended loads and complementary dissolved
425 loads of up to ~-36‰, although with an average of -22‰, similar to the results
426 here (Pogge von Strandmann et al., 2006; Vigier et al., 2009). Rivers from the
427 basaltic Azores exhibit an average $\Delta^7Li_{susp\text{-}soln}$ ~ -17 ± 7‰ (Pogge von
428 Strandmann et al., 2010), while rivers draining the Columbia River Basalts show
429 an average $\Delta^7Li_{susp\text{-}soln}$ ~ -17 ± 4‰ (Liu et al., 2015). Comparatively, alteration of
430 the fresh oceanic basalts (one of the primary sinks of Li from seawater) cause -
431 26±1‰ fractionation from solution (in this case seawater), while weathered
432 oceanic basalts exhibit -22±4‰ (Chan et al., 1992), and dredged ophiolite is
433 fractionated by ~-17‰ (Coogan et al., 2017). Even subaerial basalts, when
434 weathered by seawater, show -21‰ fractionation (Pogge von Strandmann et al.,
435 2008). Thus, while there are apparently subtle differences in fractionation
436 between different terrains (bearing in mind that riverine suspended loads do not
437 necessarily only consist of secondary minerals), observed fractionations appears
438 to be broadly similar, around ~20‰. The observed fractionation in these
439 experiments is also similar to the overall variability observed in a global
440 compilation of published riverine values (Murphy et al., 2019), and the mean
441 discharge-weighted $\delta^7Li$ of ~23‰ observed in rivers (Huh et al., 1998).
442 In several different river studies, including in basaltic terrains, Li/Na
443 ratios have been reported to have a similar behaviour as Li isotope ratios,

444 because Na is considered to be highly mobile (and hence remains in the fluid
445 phase) (Dellinger et al., 2015; Liu et al., 2015; Millot et al., 2010; Pogge von
446 Strandmann et al., 2017b). Hence, Li/Na ratios are likely also be controlled by
447 the ratio of dissolution to precipitation, and might be a good proxy for the extent
448 of water-rock interaction time.

449 The relationship between $\delta^7$Li and Li/Na has been possible to simulate
450 with isotopic fractionation models, which yield the fractionation factors that
451 might be mineral-specific (Pogge von Strandmann et al., 2017b). Hence, overall,
452 as Li/Na decreases (because Li is removed from solution relative to Na), $\delta^7$Li
453 increases. Generally it seems that most large global rivers can be simulated
454 assuming an equilibrium fractionation relationship, although global basaltic
455 rivers appear to be following more of a Rayleigh fractionation relationship
456 (Pogge von Strandmann et al., 2017b).

457 In the case of this study, the data show a logarithmic relationship between
458 Li/Na and $\delta^7$Li as it evolves from the starting point of the initial water (Fig. 6).
459 This relationship can be modelled with a Rayleigh fractionation equation, given
460 that the experiments in this study behaved as a closed system. Hence, ~90% of
461 the initial Li was taken up into various secondary phases. All the data form a
462 single fractionation relationship stemming from the initial fluid composition,
463 with a best-fit Rayleigh $\alpha$ value of 0.991 ($r^2$ = 0.96). This is generally similar to
464 fractionation factors reported during natural basalt weathering: MORB-seawater
465 and basalt particle-seawater interaction have $\alpha$~0.985 (Chan et al., 1992; Pogge
466 von Strandmann et al., 2008), and the best-fit to a global compilation of basaltic
467 rivers is to a Rayleigh relationship with $\alpha$~0.992 (Pogge von Strandmann et al.,
468 2017b). This factor is likely related both to the experimental fluid composition

469 (and hence the starting fluid composition and the composition of the basalt)
470 because it is likely to control the precise secondary mineralogy.
471
472 *4.4 Mobility and $\delta^7$Li*
473 One of the prevailing questions about the use of Li isotopes as a palaeo-
474 weathering proxy is what process precisely these isotopes are tracing. Generally
475 Li isotopes are considered to be able to trace weathering congruency (Pogge von
476 Strandmann and Henderson, 2015) or weathering intensity (Dellinger et al.,
477 2015), but not directly weathering rates (Pogge von Strandmann et al., 2017b).
478 Often in models of palaeo-records, Li isotopes are considered likely to be able to
479 act as a tracer for the riverine Li concentration and/or flux (Lechler et al., 2015;
480 Li and West, 2014; Pogge von Strandmann et al., 2017a; Pogge von Strandmann
481 et al., 2013). However, even if $\delta^7$Li were a perfect tracer for the Li flux, there is
482 little knowledge of how these fluxes might relate to those of elements critical to
483 the precipitation of marine carbonate and hence to the carbon cycle, such as Ca
484 or Mg. Hence, it has become important to determine the relationship between
485 the behaviour of Li in relation to that of Ca and Mg.
486 Elemental mobility during weathering is the tendency of a particular
487 element to go into the fluid phase versus being taken up by secondary minerals
488 during weathering. During basaltic weathering, Na is the most mobile major
489 cation (Gíslason et al., 1996), and hence the mobility of other cations is
490 commonly reported as the relative mobility to Na, where the formula is
491 $(x/Na)_{solution}/(x/Na)_{rock}$. In Icelandic basalts relatively mobile elements such as
492 Ca and Mg are approximately ~10× less mobile than Na, while immobile
493 elements such as Al or Fe are about three orders of magnitude less mobile than

494 Na (Gíslason et al., 1996). Natural studies have rarely measured Li
495 concentrations, and hence the relative difference between the weathering
496 mobility of Li and Ca or Mg remains poorly understood.
497 In the case of our experiments, the final equilibrium mobilities are similar
498 to the natural values reported by Gislason et al. (1996), but show a clear trend of
499 evolution with time. Magnesium starts at around 13× less mobile than Na, but
500 within 4 days has evolved slightly to its final value of ~11× less mobile (Fig. 7).
501 Cations such as Ca behave similarly, albeit in the case of Ca the relative mobility
502 decreases slightly with time. The relative mobility of lithium, on the other hand,
503 changes more dramatically, starting out at almost 75% of the mobility of Na, and
504 decreasing, and stabilising at, about 10% after ~100 days reaction. Over 80% of
505 this change in mobility occurs within the first month of the experiment. This
506 observation supports the hypothesis that secondary mineral formation, rather
507 than solely the more rapidly reacting exchangeable fraction, is largely affecting
508 the Li isotope composition. Exchangeable reactions take a few hours to occur
509 (Pistiner and Henderson, 2003), while the kinetics of secondary mineral
510 formation are thought to be relatively slow (on the order of $10^{-19}$ mol/cm$^2$/s
511 (Yokoyama and Banfield, 2002)). However, those observations on secondary
512 mineral kinetics were largely made using major elements, not more sensitive
513 trace elements such as Li, and our data suggest that at least amorphous
514 secondary phases begin to form within a few days.
515 From the point of using Li as a tracer of overall chemical weathering
516 processes, especially the transport of Ca and Mg to the oceans to form carbonate
517 thereby drawing down $CO_2$, the relative mobility difference between Li and Ca or
518 Mg is more revealing: Li starts the experiment as ~15× more mobile than Ca

519 (and ~9× more mobile than Mg), but these values decrease with time during the
520 experiment to Li being only 2.2× more mobile than Ca (and 1.0× as mobile as
521 Mg)(Fig. 8). This temporal evolution is almost entirely driven by the significant
522 changes in Li concentration, although there is also a relatively small decrease in
523 Ca mobility as well. Most of these change occurs within the first month of the
524 experiments, while for the subsequent >7 months significantly less changes
525 occur. The relatively slower evolution of Li mobility (compared to major
526 elements) suggests that Li may be a very sensitive element for tracing very early
527 and small amounts of incipient secondary mineral formation. Certainly
528 measurements using X-Ray Diffraction (XRD) of the pre- and post-experiment
529 basalts cannot distinguish the amounts of phyllosilicates or Fe oxides in the two
530 basalts. Hence the partitioning of Li is clearly more sensitive to the inception of
531 secondary mineral formation than XRD.
532 Equally, no discernible difference in clay-associated OH abundance could
533 be detected between the starting samples and the experimental samples using
534 Fourier-transform infrared (FTIR). This therefore also suggests that the
535 difference between pre- and post-experiment samples are small.
536 These results therefore suggest two points: 1) the changes in the phases
537 controlling the Li isotope ratios are very small, showing that $\delta^7$Li is considerably
538 more sensitive to these changes than the more standard methods of XRD and
539 FTIR; 2) once a steady-state is reached, Li has a similar mobility to both Ca and
540 Mg, meaning that Li is a useful tracer for the behaviour during weathering of
541 these two critical elements (Pogge von Strandmann et al., 2016).
542 Notably, given that only Li isotope ratios are useful in the marine
543 geological record, and not absolute Li concentrations, there is a correlation

544 between solution $\delta^7$Li and the relative mobility of Li to Ca and Li to Mg (Fig. 8). In
545 the case of Ca, the negative relationship has an $r^2$ of 0.99. After four days of
546 reaction, the Li to Ca mobility begins to decrease and $\delta^7$Li to further increase
547 (Fig. 8), again largely driven by the change in Li concentration correlating with
548 $\delta^7$Li. In other words, during the experiment, the Li/Ca and Li/Mg ratios of the
549 secondary minerals must be increasing as Li is increasingly removed from
550 solution. After a month (34 days) of reaction, the rates of change of Li to Ca
551 mobility and of $\delta^7$Li dramatically decline, as the reaction reaches apparent
552 steady-state.
553 Thus, not only does Li rapidly (from a natural weathering perspective)
554 reach a similar mobility to Ca and Mg, but also $\delta^7$Li is therefore an excellent
555 tracer of Li mobility. This is useful from the point of palaeo-reconstructions. For
556 example, speleothem reconstructions using Li isotopes have determined the Li
557 mobility over time (Pogge von Strandmann et al., 2017c). The same calculations
558 can be performed for seawater archives, assuming that both hydrothermal input
559 rates (possibly via reconstructed spreading rates), and the starting rock
560 composition of rivers are "known". Using the equilibrium Li to Ca mobility
561 (based on $\delta^7$Li) for the riverine input, it would then be possible to determine the
562 past behaviour of riverine Ca or Mg fluxes from Li isotopes. Before this can be
563 properly adopted, similar experiments are required on different primary
564 lithologies (e.g. granites, shales, etc.), but it raises the possibility of $\delta^7$Li being a
565 direct quantitative proxy for the behaviour of Ca and Mg, and hence $CO_2$
566 drawdown over geologic time.
567

## 5.0 Conclusions

Basalts were experimentally reacted with water in closed reactors for over nine months. During this time, while solution major elements such as Mg or Si increased in concentration in the fluid phase (implying basalt dissolution), dissolved Li concentrations decreased, and $\delta^7$Li increased, implying removal of Li into or sorption onto secondary phases.

Mass balance calculations using selective leaches of the pre- and post-experiment basalts, shows that, of the Li removed from solution, ~12–16% was taken up by the exchangeable fraction (imparting a ~12‰ fractionation to $\delta^7$Li), and the remainder by neoformed secondary minerals (imparting ~23‰ fractionation). For at least the final 6 months of the experiment, Li fractionation appears to have reached steady-state conditions, and isotope ratios remain approximately constant. The $\delta^7$Li vs. Li/Na trends of the experiment follow an overall closed-system Rayleigh relationship with an $\alpha = 0.991$, similar to other basaltic rivers.

The solution Li isotope ratio also correlates with the modelled saturation index of smectite, where an extrapolation of the trend to saturated conditions (SI = 0) converges towards basaltic $\delta^7$Li compositions, further implying that neoformation of secondary minerals may be largely controlling solution $\delta^7$Li. This suggests that Li isotopes are more susceptible to this early mineral formation than major element ratios, or to standard methods of clay detection such as X-Ray diffraction and Fourier-transform infrared. Equally, this implies that the onset of clay formation (or even amorphous clays) is much more rapid than initially thought (on the order of a few days to months).

Finally, the relatively mobility of Li to those cations critical in the carbon cycle (Ca and Mg) evolves with time, but rapidly (within one month) reaches a point where the behaviour of Li is broadly similarly mobile to both elements. There is also a direct correlation between $\delta^7$Li and this mobility, implying that Li isotopes can be used to trace Li mobility, and therefore can be used to trace Ca and Mg mobility (at least during basalt weathering), and ultimately $CO_2$ drawdown.

Acknowledgements

The experiments and experimental equipment were funded by Royal Society Research Grant 537708. PPvS and MJM were funded by ERC Consolidator grant 682760 CONTROLPASTCO2. We thank Ed Tipper, Josh Wimpenny and an anonymous reviewer for their comments.

Allegre, C.J. et al., 2010. The fundamental role of island arc weathering in the oceanic Sr isotope budget. Earth and Planetary Science Letters, 292(1-2): 51-56.

Berner, R.A., Lasaga, A.C., Garrels, R.M., 1983. The Carbonate-Silicate Geochemical Cycle and Its Effect on Atmospheric Carbon-Dioxide over the Past 100 Million Years. American Journal of Science, 283(7): 641-683.

Bouchez, J., von Blanckenburg, F., Schuessler, J.A., 2013. Modeling novel stable isotope ratios in the weathering zone. American Journal of Science, 313.

Chamberlin, T.C., 1899. An attempt to frame a working hypothesis of the cause of glacial periods on an atmospheric basis. Journal of Geology, 7(6): 545–584.

Chan, L.H., Edmond, J.M., Thompson, G., Gillis, K., 1992. Lithium isotopic composition of submarine basalts: implications for the lithium cycle in the oceans. Earth and Planetary Science Letters, 108(1-3): 151-160.

Chan, L.H., Hein, J.R., 2007. Lithium contents and isotopic compositions of ferromanganese deposites from the global ocean. Deep-Sea Research, 54: 1147-1162.

Chapela Lara, M., Buss, H.L., Pogge von Strandmann, P.A.E., Schuessler, J.A., Moore, O.W., 2017. The influence of critical zone processes on the Mg

626 isotope budget in a tropical, highly weathered andesitic catchment.
627 Geochimica Et Cosmochimica Acta, 202: 77–100.
628 Coogan, L.A., Gillis, K.M., Pope, M., Spence, J., 2017. The role of low-temperature
629 (off-axis) alteration of the oceanic crust in the global Li-cycle: Insights
630 from the Troodos ophiolite. Geochimica Et Cosmochimica Acta, 203: 201–
631 215.
632 Dellinger, M. et al., 2015. Riverine Li isotope fractionation in the Amazon River
633 basin controlled by the weathering regimes. Geochimica Et Cosmochimica
634 Acta, 164: 71–93.
635 Elliott, T., Thomas, A., Jeffcoate, A., Niu, Y.L., 2006. Lithium isotope evidence for
636 subduction-enriched mantle in the source of mid-ocean-ridge basalts.
637 Nature, 443(7111): 565–568.
638 Flesch, G.D., Anderson, A.R., Svec, H.J., 1973. A secondary isotopic standard for
639 6Li/7Li determinations. Int. J. Mass Spectrom. Ion Process., 12: 265–272.
640 Foster, G.L., Vance, D., 2006. Negligible glacial-interglacial variation in
641 continental chemical weathering rates. Nature, 444(7121): 918-921.
642 Gíslason, S.R., Arnorsson, S., Armannsson, H., 1996. Chemical weathering of
643 basalt in southwest Iceland: Effects of runoff, age of rocks and
644 vegetative/glacial cover. American Journal of Science, 296(8): 837–907.
645 Hawley, S.M., Pogge von Strandmann, P.A.E., Burton, K.W., Williams, H.M.,
646 Gislason, S.R., 2017. Continental weathering and terrestrial
647 (oxyhydr)oxide export: Comparing glacial and non-glacial catchments in
648 Iceland. Chemical Geology, 462: 55–66.
649 Heimburger, A. et al., 2013. SLRS-5 Elemental Concentrations of Thirty-Three
650 Uncertified Elements Deduced from SLRS-5/SLRS-4 Ratios. Geostandards
651 and Geoanalytical Research, 37(1): 77-85.
652 Hindshaw, R.S., Aciego, S.M., Tipper, E.T., 2018. Li and U Isotopes as a Potential
653 Tool for Monitoring Active Layer Deepening in Permafrost Dominated
654 Catchments. Frontiers in Earth Science, 6.
655 Hindshaw, R.S. et al., 2019. Experimental constraints on Li isotope fractionation
656 during clay formation. Geochimica Et Cosmochimica Acta, 250: 219–237.
657 Huh, Y., Chan, L.H., Zhang, L., Edmond, J.M., 1998. Lithium and its isotopes in
658 major world rivers: Implications for weathering and the oceanic budget.
659 Geochimica Et Cosmochimica Acta, 62(12): 2039–2051.
660 James, R.H., Palmer, M.R., 2000. The lithium isotope composition of international
661 rock standards. Chemical Geology, 166(3-4): 319-326.
662 Jeffcoate, A.B., Elliott, T., Thomas, A., Bouman, C., 2004. Precise, small sample size
663 determinations of lithium isotopic compositions of geological reference
664 materials and modern seawater by MC-ICP-MS. Geostandards and
665 Geoanalytical Research, 28(1): 161-172.
666 John, T. et al., 2012. Volcanic arcs fed by rapid pulsed fluid flow through
667 subducting slabs Nature Geoscience, 5: 489–492.
668 Jones, M.T., Pearce, C.R., Oelkers, E.H., 2012. An experimental study of the
669 interaction of basaltic riverine particulate material and seawater.
670 Geochimica Et Cosmochimica Acta, 77: 108–120.
671 Kisakürek, B., James, R.H., Harris, N.B.W., 2005. Li and $\delta^7$Li in Himalayan rivers:
672 Proxies for silicate weathering? Earth and Planetary Science Letters,
673 237(3-4): 387–401.

674 Lechler, M., Pogge von Strandmann, P.A.E., Jenkyns, H.C., Prosser, G., Parente, M.,
675 2015. Lithium-isotope evidence for enhanced silicate weathering during
676 OAE 1a (Early Aptian Selli event). Earth and Planetary Science Letters,
677 432: 210–222.
678 Lemarchand, E., Chabaux, F., Vigier, N., Millot, R., Pierret, M.C., 2010. Lithium
679 isotope systematics in a forested granitic catchment (Strengbach, Vosges
680 Mountains, France). Geochimica Et Cosmochimica Acta, 74: 4612-4628.
681 Li, G., West, A.J., 2014. Evolution of Cenozoic seawater lithium isotopes: Coupling
682 of global denudation regime and shifting seawater sinks. Earth and
683 Planetary Science Letters, 401: 284–293.
684 Liu, X.-L., Rudnick, R.L., McDonough, W.F., Cummings, M.L., 2013. Influence of
685 chemical weathering on the composition of the continental crust: Insights
686 from Li and Nd isotopes in bauxite profiles developed on Columbia River
687 Basalts. Geochimica Et Cosmochimica Acta, 115: 73–91.
688 Liu, X.-M., Wanner, C., Rudnick, R.L., McDonough, W.F., 2015. Processes
689 controlling δ7Li in rivers illuminated by study of streams and
690 groundwaters draining basalts. Earth and Planetary Science Letters, 409:
691 212–224.
692 Magna, T., Wiechert, U., Halliday, A.N., 2006. New constraints on the lithium
693 isotope compositions of the Moon and terrestrial planets. Earth and
694 Planetary Science Letters, 243(3-4): 336-353.
695 Maher, K., 2011. The role of fluid residence time and topographic scales in
696 determining chemical fluxes from landscapes. Earth and Planetary
697 Science Letters, 312: 48–58.
698 McArthur, J.M., Howarth, R.J., Bailey, T.R., 2001. Strontium isotope stratigraphy:
699 LOWESS version 3: Best fit to the marine Sr-isotope curve for 0-509 Ma
700 and accompanying look-up table for deriving numerical age. Journal of
701 Geology, 109(2): 155-170.
702 Millot, R., Girard, J.P., 2007. Lithium Isotope Fractionation during adsorption
703 onto mineral surfaces, International meeting, Clays in natural &
704 engineered barriers for radioactive waste confinement, Lille, Frace.
705 Millot, R., Vigier, N., Gaillardet, J., 2010. Behaviour of lithium and its isotopes
706 during weathering in the Mackenzie Basin, Canada. Geochimica Et
707 Cosmochimica Acta, 74: 3897–3912.
708 Misra, S., Froelich, P.N., 2012. Lithium Isotope History of Cenozoic Seawater:
709 Changes in Silicate Weathering and Reverse Weathering. Science, 335:
710 818–823.
711 Murphy, M.J. et al., 2019. Tracing silicate weathering processes in the
712 permafrost-dominated Lena River watershed using lithium isotopes.
713 Geochimica Et Cosmochimica Acta, 245: 154–171.
714 Oliver, L. et al., 2003. Silicate weathering rates decoupled from the $^{87}Sr/^{86}Sr$ ratio
715 of the dissolved load during Himalayan erosion. Chemical Geology, 201(1-
716 2): 119–139.
717 Opfergelt, S. et al., 2014. Magnesium retention on the soil exchange complex
718 controlling Mg isotope variations in soils, soil solutions and vegetation in
719 volcanic soils, Iceland. Geochimica Et Cosmochimica Acta, 125: 110–130.
720 Parkhurst, D.L., Appelo, C.A.J., 1999. User's guide to PHREEQC (version 2) - a
721 computer program for speciation, batch-reaction, one-dimensional
722 transport, and inverse geochemical calculations.

723 Penniston-Dorland, S., Liu, X.-M., Rudnick, R.L., 2017. Lithium Isotope
724 Geochemistry, Rev. Min. Geochem., pp. 165–217.
725 Phan, T.T. et al., 2016. Factors controlling Li concentration and isotopic
726 composition in formation waters and host rocks of Marcellus Shale,
727 Appalachian Basin. Chemical Geology, 420: 162–179.
728 Pistiner, J.S., Henderson, G.M., 2003. Lithium-isotope fractionation during
729 continental weathering processes. Earth and Planetary Science Letters,
730 214(1-2): 327-339.
731 Pogge von Strandmann, P.A.E., Burton, K.W., James, R.H., van Calsteren, P.,
732 Gislason, S.R., 2010. Assessing the role of climate on uranium and lithium
733 isotope behaviour in rivers draining a basaltic terrain. Chemical Geology,
734 270: 227–239.
735 Pogge von Strandmann, P.A.E. et al., 2006. Riverine behaviour of uranium and
736 lithium isotopes in an actively glaciated basaltic terrain. Earth and
737 Planetary Science Letters, 251: 134–147.
738 Pogge von Strandmann, P.A.E. et al., 2016. The effect of hydrothermal spring
739 weathering processes and primary productivity on lithium isotopes: Lake
740 Myvatn, Iceland. Chemical Geology, 445: 4–13.
741 Pogge von Strandmann, P.A.E. et al., 2017a. Global climate stabilisation by
742 chemical weathering during the Hirnantian glaciation. Geochemical
743 Perspective Letters, 3: 230–237.
744 Pogge von Strandmann, P.A.E. et al., 2011. Variations of Li and Mg isotope ratios
745 in bulk chondrites and mantle xenoliths. Geochimica Et Cosmochimica
746 Acta, 75: 5247–5268.
747 Pogge von Strandmann, P.A.E., Frings, P.J., Murphy, M.J., 2017b. Lithium isotope
748 behaviour during weathering in the Ganges Alluvial Plain. Geochimica Et
749 Cosmochimica Acta, 198: 17–31.
750 Pogge von Strandmann, P.A.E., Henderson, G.M., 2015. The Li isotope response to
751 mountain uplift. Geology, 43(1): 67–70.
752 Pogge von Strandmann, P.A.E., James, R.H., van Calsteren, P., Gíslason, S.R.,
753 Burton, K.W., 2008. Lithium, magnesium and uranium isotope behaviour
754 in the estuarine environment of basaltic islands. Earth and Planetary
755 Science Letters, 274(3-4): 462-471.
756 Pogge von Strandmann, P.A.E., Jenkyns, H.C., Woodfine, R.G., 2013. Lithium
757 isotope evidence for enhanced weathering during Oceanic Anoxic Event 2.
758 Nature Geoscience, 6: 668–672.
759 Pogge von Strandmann, P.A.E. et al., 2012. Lithium, magnesium and silicon
760 isotope behaviour accompanying weathering in a basaltic soil and pore
761 water profile in Iceland. Earth and Planetary Science Letters, 339–340:
762 11–23.
763 Pogge von Strandmann, P.A.E. et al., 2014. Chemical weathering processes in the
764 Great Artesian Basin: Evidence from lithium and silicon isotopes. Earth
765 and Planetary Science Letters, 406: 24–36.
766 Pogge von Strandmann, P.A.E. et al., 2017c. Lithium isotopes in speleothems:
767 Temperature-controlled variation in silicate weathering during glacial
768 cycles. Earth and Planetary Science Letters, 469: 64–74.
769 Renforth, P., Pogge von Strandmann, P.A.E., Henderson, G.M., 2015. The
770 dissolution of olivine added to soil: Implications for enhanced weathering.
771 Applied Geochemistry, 61: 109–118.

Sauzeat, L., Rudnick, R.L., Chauvel, C., Garcon, M., Tang, M., 2015. New perspectives on the Li isotopic composition of the upper continental crust and its weathering signature. Earth and Planetary Science Letters, 428: 181–192.

Sigfusson, B., Gislason, S.R., Paton, G.I., 2008. Pedogenesis and weathering rates of a Histic Andosol in Iceland: Field and experimental soil solution study. Geoderma, 144(3-4): 572-592.

Tessier, A., Campbell, P.G.C., Bisson, M., 1979. Sequential Extraction Procedure for the Speciation of Particulate Trace Metals. Analytical Chemistry, 51(7): 844-851.

Vance, D., Teagle, D.A.H., Foster, G.L., 2009. Variable Quaternary chemical weathering fluxes and imbalances in marine geochemical budgets. Nature, 458: 493–496.

Vigier, N. et al., 2008. Quantifying Li isotope fractionation during smectite formation and implications for the Li cycle. Geochimica Et Cosmochimica Acta, 72: 780–792.

Vigier, N., Gislason, S.R., Burton, K.W., Millot, R., Mokadem, F., 2009. The relationship between riverine lithium isotope composition and silicate weathering rates in Iceland. Earth and Planetary Science Letters, 287(3-4): 434–441.

Walker, J.C.G., Hays, P.B., Kasting, J.F., 1981. A Negative Feedback Mechanism for the Long-Term Stabilization of Earths Surface-Temperature. Journal of Geophysical Research-Oceans and Atmospheres, 86(NC10): 9776-9782.

West, A.J., Galy, A., Bickle, M., 2005. Tectonic and climatic controls on silicate weathering. Earth and Planetary Science Letters, 235(1-2): 211–228.

Wimpenny, J. et al., 2015. Lithium isotope fractionation during uptake by gibbsite. Geochimica Et Cosmochimica Acta, 168: 133–150.

Wimpenny, J. et al., 2010. The behaviour of Li and Mg isotopes during primary phase dissolution and secondary mineral formation in basalt. Geochimica Et Cosmochimica Acta, 74: 5259-5279.

Yokoyama, T., Banfield, J.F., 2002. Direct determinations of the rates of rhyolite dissolution and clay formation over 52,000 years and comparison with laboratory measurements. Geochimica Et Cosmochimica Acta, 66: 2665–2681.

| Sample | Time days | pH | Na mg/L | Mg mg/L | Al µg/L | Si mg/L | K mg/L | Ca mg/L | Li µg/L | $\delta^7$Li ‰ | 2sd |
|---|---|---|---|---|---|---|---|---|---|---|---|
| Initial water | 0 | 6.84 | 48.5 | 7.87 | b.d.l. | 2.59 | 11.1 | 11.8 | 13.5 | 14.7 | 0.4 |
| 15.1 | 1 | 6.91 | 47.8 | 9.28 | 8.50 | 3.19 | 9.63 | 11.9 | 9.9 | 15.8 | 0.1 |
| 15.2 | 2 | 6.86 | 48.4 | 9.92 | 5.58 | 3.41 | 9.32 | 11.5 | 9.9 | 16.8 | 0.5 |
| 15.3 | 4 | 6.89 | 48.4 | 10.6 | 8.65 | 3.61 | 8.95 | 11.0 | 8.2 | 19.6 | 0.2 |
| 15.4 | 12 | 7.17 | 48.6 | 10.9 | 11.7 | 4.22 | 8.67 | 10.8 | 4.7 | 26.2 | 0.3 |
| 15.5 | 34 | 7.60 | 48.8 | 11.2 | 10.7 | 4.83 | 8.56 | 10.6 | 2.9 | 31.0 | 0.2 |
| 15.6 | 68 | 7.33 | 48.9 | 11.2 | 10.7 | 5.20 | 8.46 | 10.6 | 2.2 | 32.7 | 0.4 |
| 15.7 | 126 | 7.08 | 48.7 | 11.4 | 12.3 | 5.71 | 8.35 | 10.8 | 1.6 | 34.4 | 0.3 |
| 15.8 | 252 | 7.04 | 49.4 | 11.5 | 11.7 | 6.18 | 8.35 | 10.8 | 1.3 | 33.3 | 0.3 |
| 16.1 | 1 | 7.26 | | | | | | | 9.5 | 15.4 | 0.3 |
| 16.2 | 2 | 7.05 | | | | | | | 9.5 | 16.0 | 0.5 |
| 16.3 | 4 | 7.13 | | | | | | | 8.0 | 19.6 | 0.6 |
| 16.4 | 12 | 7.43 | | | | | | | 4.8 | 24.1 | 0.4 |
| 16.5 | 34 | 7.49 | | | | | | | 2.8 | 31.5 | 0.1 |
| 16.6 | 68 | 7.29 | | | | | | | 2.3 | 33.2 | 0.1 |
| 16.7 | 126 | 7.16 | | | | | | | 1.4 | 34.9 | 0.4 |
| 16.8 | 252 | 7.31 | | | | | | | 1.4 | 33.3 | 0.4 |

Table 1. Concentration and isotope ratios from the experimental fluids.

812

813

| | Sample | $\delta^7$Li ‰ | 2sd | Li in experiment µg | Mg/Si | Ca/Si | K/Si | Li/Si | Al/Si | Fe/ |
|---|---|---|---|---|---|---|---|---|---|---|
| ole | Exp 15 | 21.3 | 0.4 | 2.47 | 9.47 | 113 | 12.6 | 0.030 | | |
| | Exp 16 | 21.8 | 0.5 | 2.90 | 8.24 | 96.4 | 10.4 | 0.015 | | |
| | Unreacted | 17.8 | 0.1 | 1.10 | 25.3 | 104 | 9.3 | 0.038 | | |
| | Exp 15 | 9.3 | 0.6 | 27.5 | 0.271 | 0.439 | 0.014 | 0.0003 | 0.567 | 0.8 |
| | Exp 16 | 10.8 | 0.1 | 27.0 | 0.292 | 0.426 | 0.013 | 0.0002 | 0.634 | 0.9 |
| | Unreacted | 5.3 | 0.5 | 17.6 | 0.294 | 0.426 | 0.013 | 0.0005 | 0.635 | 0.9 |
| | Exp 15 | 4.5 | 0.2 | 1320 | | | | | | |
| | Exp 16 | 4.1 | 0.3 | 1390 | | | | | | |
| | Unreacted | 4.4 | 0.2 | 1380 | 0.269 | 0.590 | 0.020 | 0.00003 | 0.358 | 0.5 |

Table 2. Li amounts and isotope ratios, as well as elemental ratios, from the different leached and bulk phases. Sec. mins. stands for secondary minerals.

814

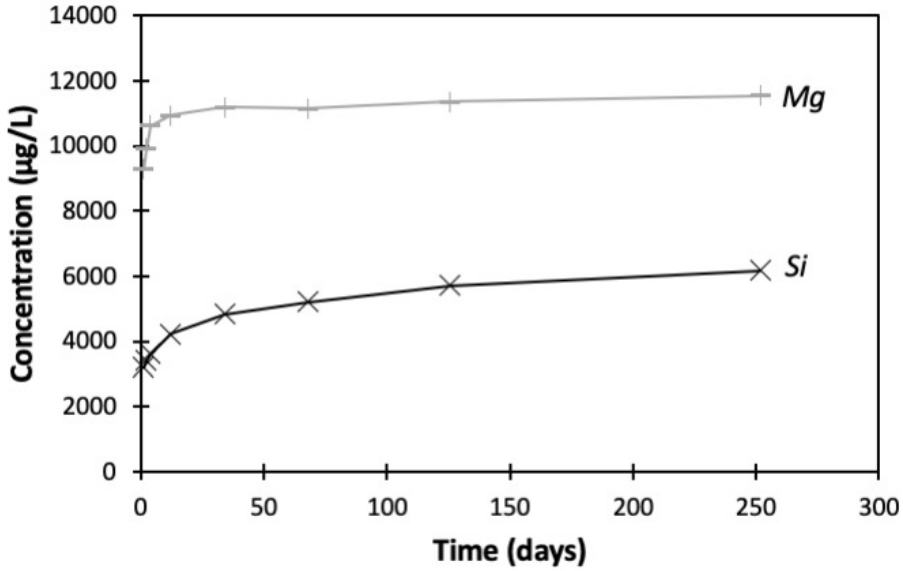


815

816 Figure 1. Measured aqueous Mg and Si concentrations during the experiment.

817 Analytical uncertainty is smaller than the symbol sizes.

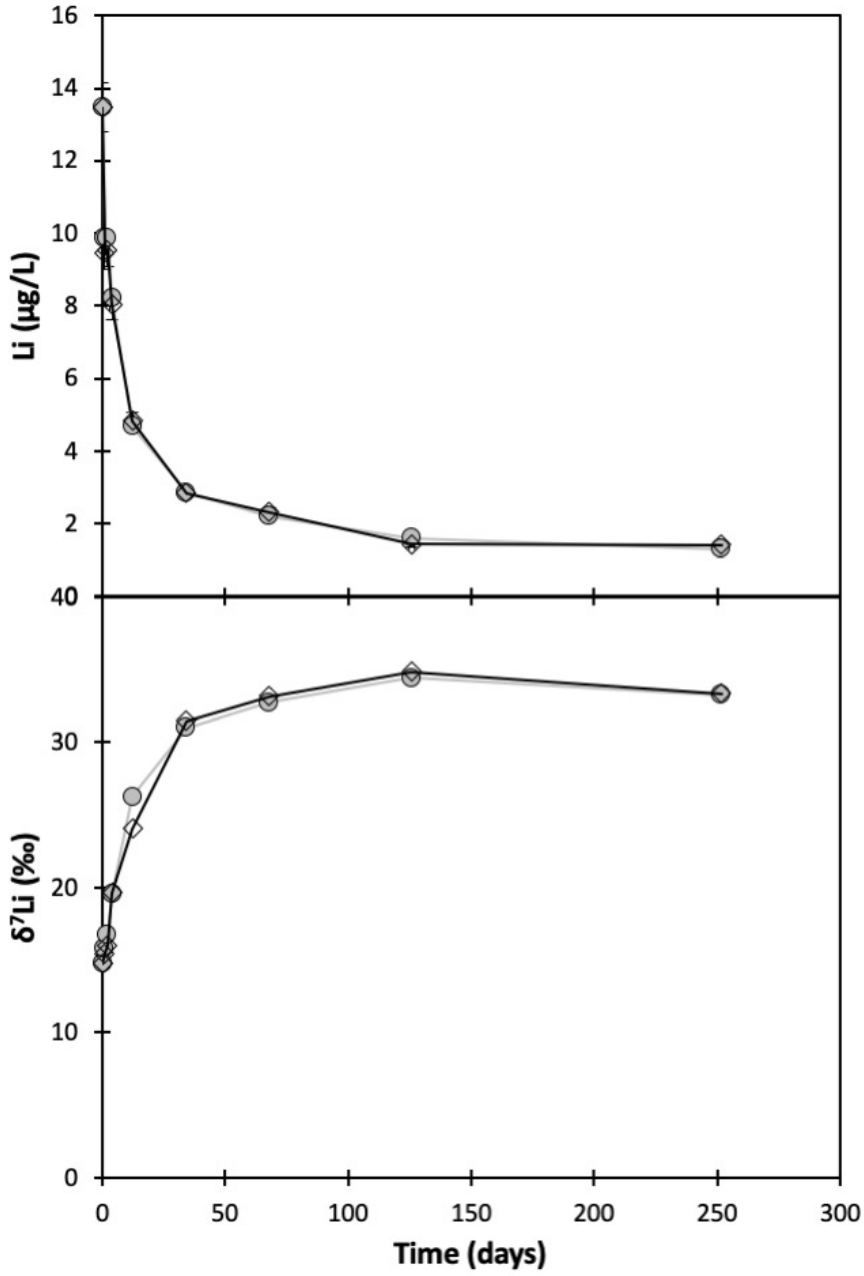


818

819 Figure 2. Solution Li concentrations and isotope ratios with time throughout the

820 experiment. The open diamonds and filled circles represent the two different

821 experiments. Analytical uncertainty is smaller than the symbol sizes.

822

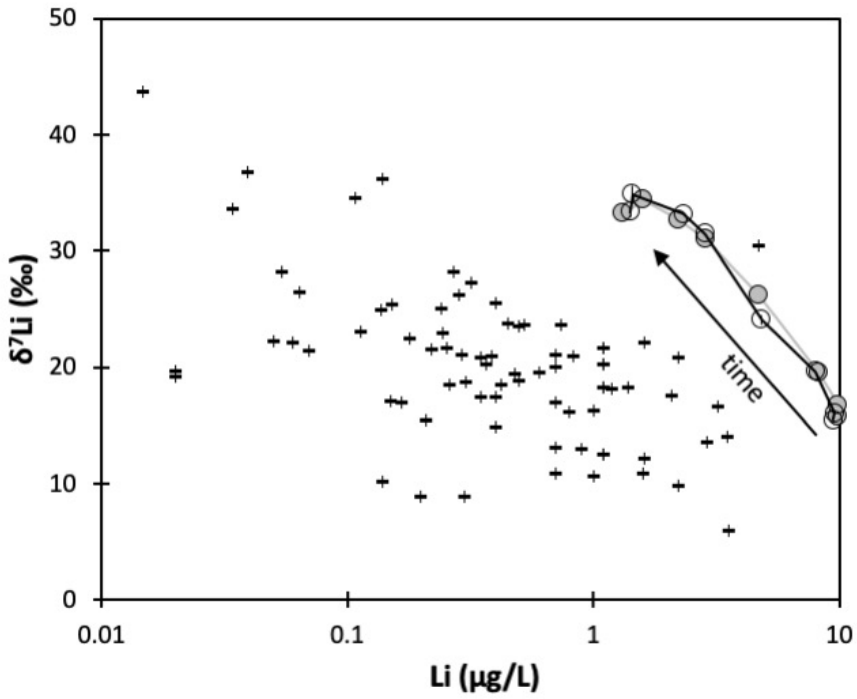


823

824 Figure 3. Measured Li isotopes ratios of the fluid phase from both experiments as
825 a function of the corresponding Li concentration. The grey and black lines
826 represent the two experiments. The black crosses are natural basaltic river
827 studies (Liu et al., 2015; Pogge von Strandmann et al., 2010; Pogge von
828 Strandmann et al., 2006; Vigier et al., 2009). Analytical uncertainty is smaller
829 than the symbol sizes.

830

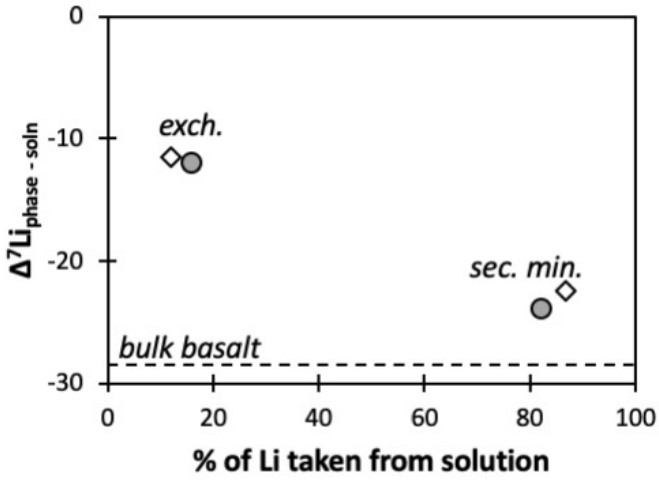


831

832 Figure 4. The mass balance of Li removed from solution by the different phases,
833 relative to the isotope fractionation from the experimental solution. The filled
834 circles represent Experiment 15, and the open diamonds Experiment 16.

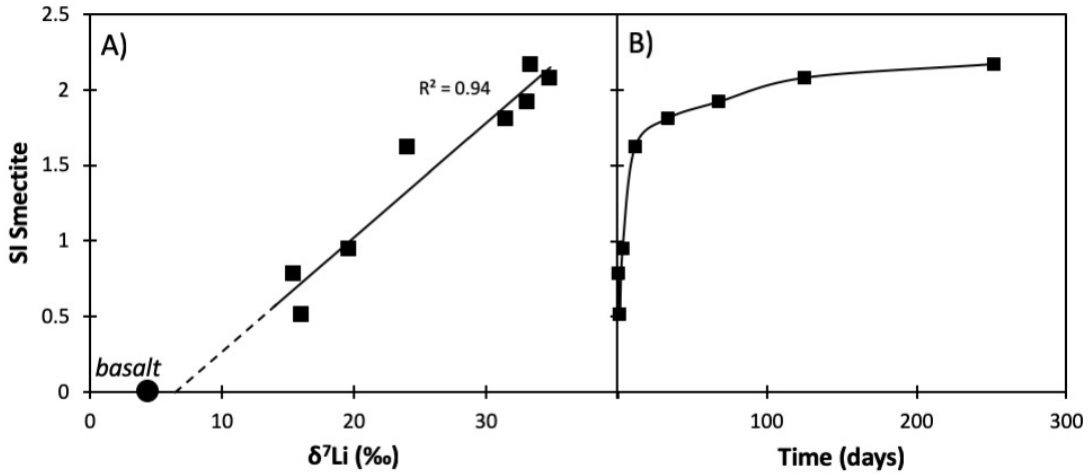


835

836 Figure 5. A) Li isotopes in solution as a function of PHREEQC-modelled smectite
837 saturation index. The dotted line is the extrapolated trend line to saturated
838 conditions. B) Trend of smectite saturation index with time during the
839 experiment.

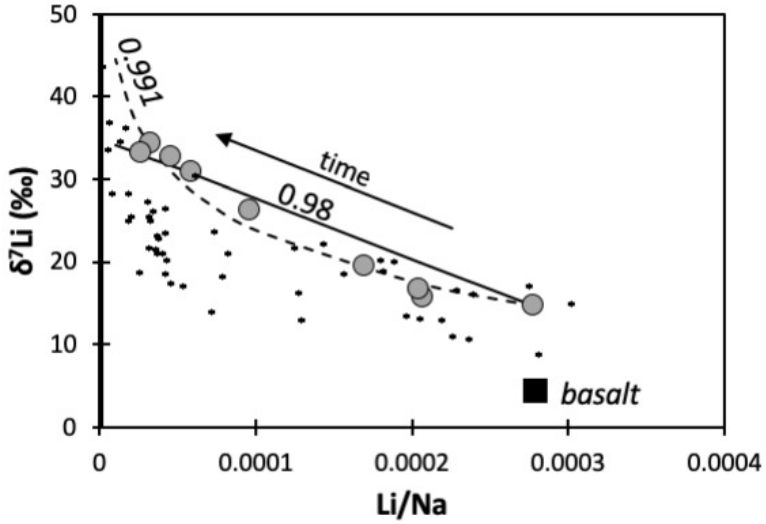


840

841 Figure 6. Experiment fluid $\delta^7$Li as a function of corresponding mass Li/Na ratio
842 (grey circles). The dotted illustrates a Rayleigh fractionation relationship, while
843 the solid line represents an equilibrium fractionation relationship. The numbers

844 next to the lines are the isotopic fractionation factors. The black crosses are
845 natural basaltic river studies (Liu et al., 2015; Pogge von Strandmann et al., 2010;
846 Pogge von Strandmann et al., 2006; Vigier et al., 2009). Analytical uncertainty is
847 smaller than the symbol sizes.
848

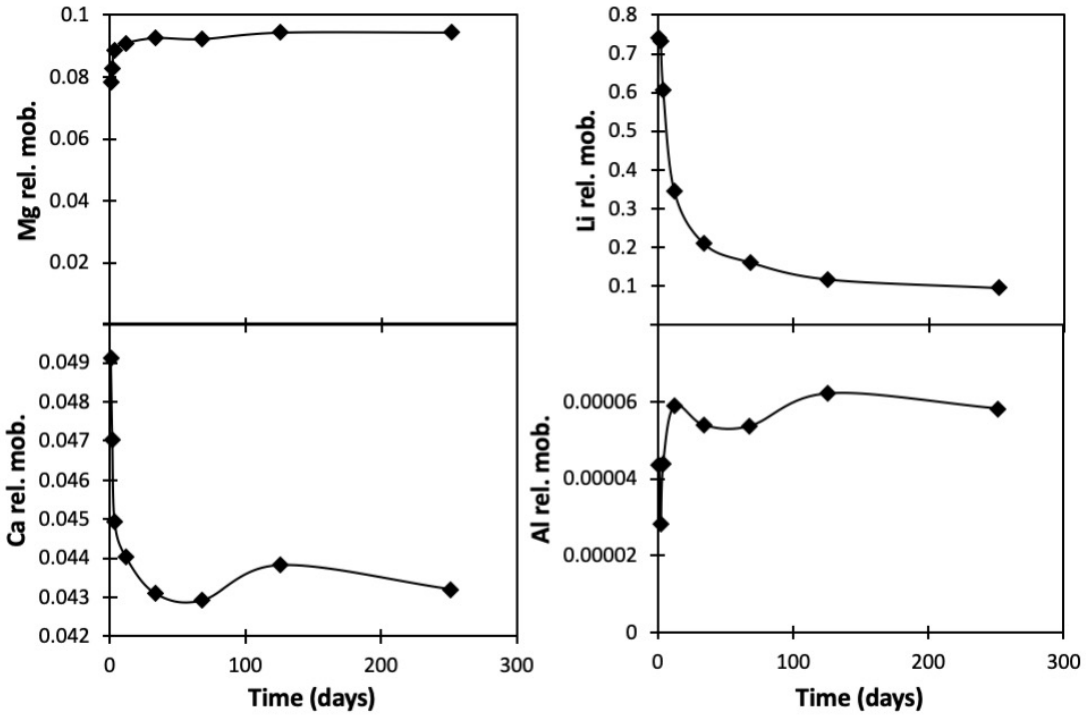


849

850 Figure 7. Relative mobility (relative to Na) of Mg, Li, Ca and Al with time through
851 the experiment. Note different scale on axes.
852

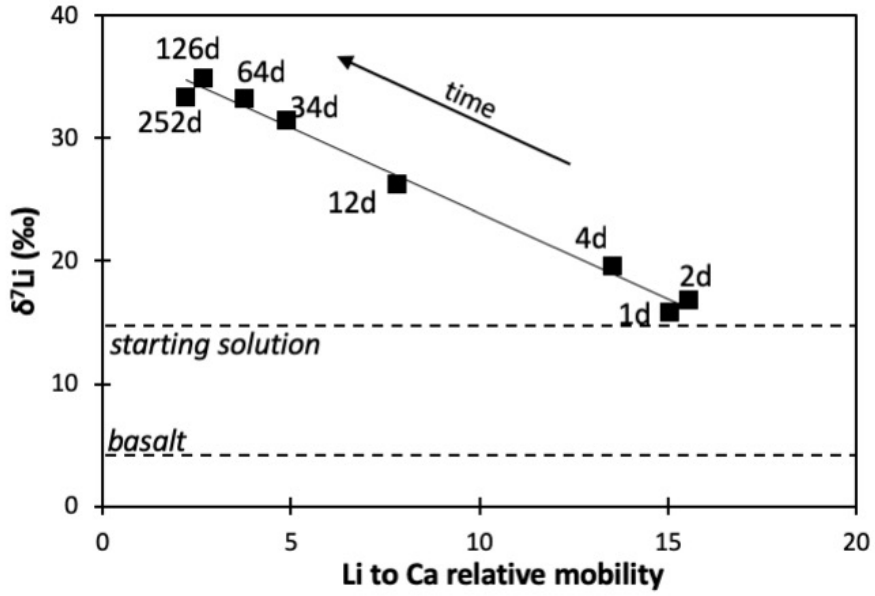


853

854 Figure 8. The reactive fluid Li isotopes ratio compared to the relative mobility of

855 Li to Ca. The numbers next to each data point represent the experimental time

856 (in days). Analytical uncertainty is smaller than the symbol sizes.

857

858

859

860

861